Automated acquisition and analysis of airway surface liquid height by confocal microscopy

Hyun-Chul Choi,[1]* Christine Seul Ki Kim,[2]* and Robert Tarran[2]

[1]*Department of Electronic Engineering, Yeungnam University, Kyungsan, Kyungbuk, South Korea; and* [2]*Cystic Fibrosis Center/Marsico Lung Institute, University of North Carolina, Chapel Hill, North Carolina*

Choi HC, Kim CS, Tarran R. Automated acquisition and analysis of airway surface liquid height by confocal microscopy. *Am J Physiol Lung Cell Mol Physiol* 309: L109–L118, 2015. First published May 22, 2015; doi:10.1152/ajplung.00027.2015.—The airway surface liquid (ASL) is a thin-liquid layer that lines the luminal side of airway epithelia. ASL contains many molecules that are involved in primary innate defense in the lung. Measurement of ASL height on primary airway cultures by confocal microscopy is a powerful tool that has enabled researchers to study ASL physiology and pharmacology. Previously, ASL image acquisition and analysis were performed manually. However, this process is time and labor intensive. To increase the throughput, we have developed an automatic ASL measurement technique that combines a fully automated confocal microscope with novel automatic image analysis software that was written with image processing techniques derived from the computer science field. We were able to acquire *XZ* ASL images at the rate of ~1 image/s in a reproducible fashion. Our automatic analysis software was able to analyze images at the rate of ~32 ms/image. As proofs of concept, we generated a time course for ASL absorption and a dose response in the presence of SPLUNC1, a known epithelial sodium channel inhibitor, on human bronchial epithelial cultures. Using this approach, we determined the IC_{50} for SPLUNC1 to be 6.53 μM. Furthermore, our technique successfully detected a difference in ASL height between normal and cystic fibrosis (CF) human bronchial epithelial cultures and detected changes in ATP-stimulated Cl^-/ASL secretion. We conclude that our automatic ASL measurement technique can be applied for repeated ASL height measurements with high accuracy and consistency and increased throughput.

cystic fibrosis; COPD; CFTR; ENaC; fluorescent microscopy; airway surface liquid

THE AIRWAY SURFACE LIQUID (ASL) is a thin layer of salt, water, and protein that lines the respiratory tract and facilitates innate immunity in the lung. ASL is comprised of two layers, one that is directly adjacent to the epithelial cells, which is called the periciliary liquid layer (PCL), and another, called the mucus layer, which lies on top of the PCL (17, 24, 36). Maintaining hydrated ASL is important to provide a low-viscosity environment for cilia to beat effectively and to propel mucus, pathogens, and particles toward the mouth (5, 17, 36, 38). Furthermore, dehydrated ASL accelerates the development of mucus plugs, which can obstruct air flow and serve as focal points for bacterial colonization (4, 8, 17, 36, 42). ASL hydration is controlled by the transepithelial movement of ions and water (5, 6, 17, 36). At the apical membrane of airway epithelia, anions are mostly secreted by CFTR and Na^+ is absorbed by the epithelial sodium channel (ENaC) (5, 17, 23, 33, 36). In the

case of cystic fibrosis (CF), where CFTR is mutated and has disrupted or diminished function, the balance between anion secretion and Na^+ absorption is altered (5, 6, 17, 23, 36, 38). An absence of functioning CFTR leads to reduced anion secretion and triggers hyperactive ENaC that excessively absorbs Na^+, which together leads to dehydrated ASL (1, 5, 17, 36). Whereas calcium-activated chloride channels (CaCCs) are functional in CF airways, CaCC activity is short lived and therefore cannot compensate fully for the loss of CFTR function in CF airways (29, 31). Consequently, ASL dehydration impairs mucociliary clearance and results in chronic bacterial infection of the lung (4, 8, 17, 23, 36, 42).

Measuring the ASL height has served as a useful tool to study ASL physiology pertaining to ASL volume, ionic movement, and mucus transport. Previously, ASL height measurements have been used to show that PCL transport is dependent on mucus transport (20, 21, 29). Also, studies on ASL absorption rates using ASL measurements revealed the importance of restoring ASL volume to treat dehydrated airway in CF and chronic obstructive pulmonary disease (COPD) (3, 12, 15, 30). Moreover, the function of ENaC and CFTR and ASL hydration was studied by using ASL measurements (11, 15, 26, 41). Different ASL mediators that alter ENaC activity such as channel-activating proteases (CAP), CAP inhibitors, ATP, ADO, and SPLUNC1 have all been assessed by using ASL height measurements (12, 14, 31). ASL measurements were also used to evaluate the efficacy of pharmacological agents such as drugs from Vertex including Ivacaftor and Lumacaftor for CF lung disease (34, 35).

A variety of methodologies have been proposed and used to measure ASL height. Light and electron microscopy techniques have been used to measure ASL in airways fixed in situ (40). A potential drawback of this method is that adding of fixatives during the sample preparation process may alter the ASL. For an alternative model, an in vitro well-differentiated cell culture system has been adopted to measure native ASL in live cells (10, 20). Using this system, several methods have been proposed to measure ASL height: The surface laser reflectance microscopy method takes reflections of laser light to reconstruct an image of the mucosal surface (32). Light refraction microscopy measures refraction of light created by fluid meniscus to determine the volume of the meniscus at the interface between the culture and the wall of the culture insert (13). Optical coherence tomography (OCT) measures the thickness of the ASL based on the reflectance of sample. This method requires micro-OCT instrument that produces cross-sectional images with 1-μm resolution (19). Confocal microscopy offers another direct and noninvasive method for measuring ASL. This method has previously been described in detail (27, 39). In brief, ASL is labeled with an ASL-permeable

* H.-C. Choi and C. S. K. Kim contributed equally to this manuscript.

Address for reprint requests and other correspondence: R. Tarran, Cystic Fibrosis Center/Marsico Lung Institute, 7125 Thurston Bowles Bldg., UNC, Chapel Hill, NC 27599-7284 (e-mail: tarran@med.unc.edu).

but epithelium-impermeable 10-kDa dextran conjugated with a fluorophore. Images of fluorescent-labeled ASL are obtained by *XZ* scanning with a confocal microscope. Acquired images are analyzed to determine ASL height, which reflects the hydration state of ASL.

Previously, ASL height measurements were performed manually (12, 28). That is, for each culture, images were acquired at certain locations by moving the microscope stage by hand. Images were then analyzed manually by selecting the region of interest around the ASL by eye to obtain ASL height values in micrometers. However, this method is labor intensive and time consuming, which together limit the throughput. Here, we propose and outline an automatic ASL measurement method that uses an automated stage on a confocal microscope to acquire images and automatic image analysis technique to make consistent and accurate ASL height measurements in a high-speed manner.

METHODS

Primary HBECs. Human bronchial epithelial cultures (HBECs) were obtained from freshly excised bronchial specimens from normal and CF subjects ($n = 4$ donors for each type) and were harvested by enzymatic digestion as previously described under a protocol approved by the University of North Carolina Institutional Review Board (10). HBECs were cultured at an air-liquid interface in a modified bronchial epithelial growth medium with 5% CO_2 at 37°C and were used 3–4 wk after the seeding on 12-mm T-clear inserts (Corning-Costar, Corning, NY). During image acquisition, HBECs were maintained in a modified Ringer solution as described previously (29).

Confocal microscopy measurement of ASL. ASL labeling with fluorescent dextrans was performed as described previously (27, 39).

Briefly, PBS (20 μl) with 0.5 mg/ml of 10 kDa dextran-tetramethylrhodamine (Life Technologies, D-1817) was added to each culture. Perfluorocarbon (3M Fluorient FC-770) was added apically to prevent ASL evaporation. In most cases, images were then obtained in *XZ*-scanning mode by using a Leica SP8 confocal microscope with a ×63/1.3 numerical aperture (NA) glycerol immersion lens (e.g., for the SPLUNC1 time-course and dose-response experiments). ASL images were acquired by using an automatic stage with the "Mark-and-Find" function, which is available for use in the Leica LAS AF Application Suite. With this function, one can preset multiple *XY* locations and the automatic stage then moves the culture to each stored location to acquire images. We then used our proposed automatic image acquisition and analysis methods. ASL height values from all the acquired images per culture were averaged to yield an $n = 1$. In some cases, a Zeiss LSM 510 confocal microscope and a ×40/1.2 NA water immersion lens was used (e.g., for the ATP stimulation experiments and the comparison between normal and CF HBECs). The Zeiss 510 was not equipped with an automatic stage, and in this case five images per culture were obtained manually, as previously described (31).

ATP stimulation and SPLUNC1 time course and dose response. HBECS were cultured at the air-liquid interface for 3–4 wk. At 24 h before the experiment, apical mucus was removed by washing the mucosal surface with PBS for 30 min at 37°C. For the SPLUNC1 exposures, endogenous SPLUNC1 was removed 2 h before the experiment by incubating the HBECs' apical surfaces with PBS at 37°C for 30 min, after which time all additional PBS was aspirated away from the surface. For the time-course experiments, 10 μM of SPLUNC1 and dextran-tetramethylrhodamine in PBS were added apically, and ASL height was measured immediately and at additional, timed intervals with the cultures being returned to the 37°C incubator between time points. For the dose-response experiment, 0.1–100 μM of SPLUNC1 in PBS was added apically and the cultures
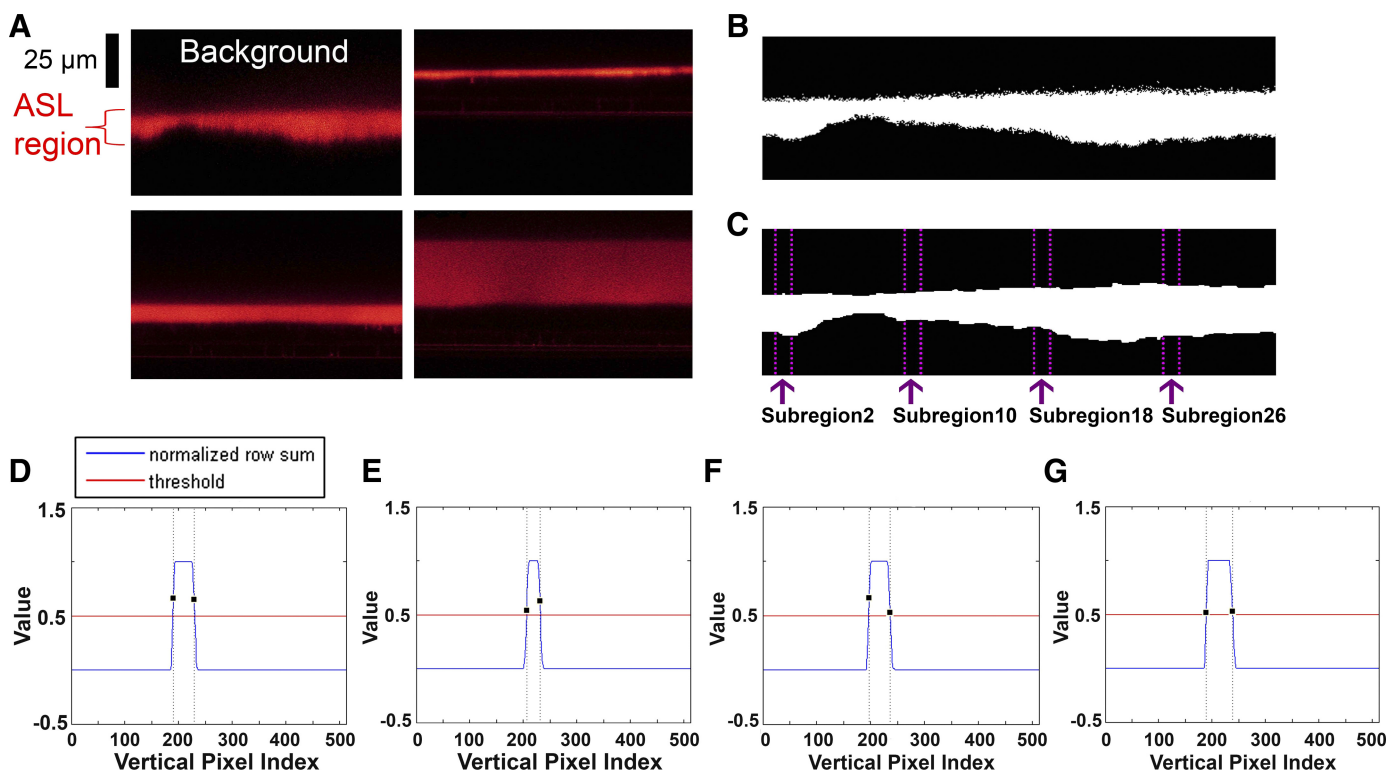

Fig. 1. Initial processing of confocal micrographs using Otsu's threshold. *A*: representative fluorescent airway surface liquid (ASL) images. The red-colored band represents the ASL region. ASL height is measured in pixels and converted into a real length according to the ratio of pixel-to-length. In this case, 512 pixels = 145 μm. Images can have an ASL region of varying height from a narrow band (*top right*) to a wide band (*bottom right*). *B*: binarized image taken from *A* (*top left*). *C*: binarized image taken from *B* after morphological operations with several subsections of the ASL region labeled. *D–G*: histogram profiles of the subsections of ASL regions shown in *C*.

were incubated at 37°C for 4 h and ASL heights were then measured. Recombinant human SPLUNC1 was purified from *Escherichia coli* as previously described (12). In some cases, cultures were preloaded with dextran-tetramethylrhodamine 24 h earlier, and then on the day of the experiment 300 μm ATP was added as a dry powder suspended in perfluorocarbon as described previously (30).

Statistical analyses. All ASL height measurements were first subjected to the D'Agostino and Pearson omnibus normality test. Since not all ASL height data sets were normally distributed, we performed the nonparametric Kruskal-Wallis test followed by Dunn's test for multiple comparisons among the time points or the dose treatments. SPLUNC1 time-course and dose-response experiments and ATP stimulation experiments are reported as means ± SE. Figure 6B analyzes the overall performance of the technique and therefore is reported as mean ± SD. $P < 0.05$ was considered statistically significant.

RESULTS

Automatic binarizing of images and finding boundaries of image subsections. To test the proposed measuring technique, we gathered 212 fluorescent images of ASL. The image size was 512^2 pixels, which corresponded to an actual area of 145 μm^2. This image set included ASL heights that widely varied from very narrow to very wide (see Fig. 1A). Our measurement algorithm consisted of two main image processing techniques. The first one was Otsu's threshold (22), which uses an adaptive

threshold to binarize an image and obtain a region of interest called the "foreground" with the other region being called the "background." Here, "adaptive" means optimal to differentiate foreground from background under various conditions of brightness and contrast. In Otsu's method, an adaptive threshold is found by exhaustively searching the threshold of maximal interclass variance or minimal intraclass variance between background and foreground. In an *XZ*-scanned fluorescent ASL image, the foreground was the red-colored ASL region and the background was in black (Fig. 1A). So the red ASL region was selected and applied with Otsu's threshold. Figure 1A shows a binarized image after applying Otsu's threshold. Since the obtained ASL images are in 8-bit images, the minimum pixel value of 0 and the maximum pixel value of 255 are used to distinctively select the background and the foreground. A binarized image with noisy edges may result in an inaccurate detection of boundaries in the additional processing steps (Fig. 1B). Therefore, to smooth out the ASL boundaries, we selected a series of morphological operations, which consisted of two iterations of dilation and three iterations of erosion, with dilation and erosion being two basic operations that are commonly used for image processing to detect edges, remove noise, and enhance images (7). In this case, they were used to describe the turning on and off of the pixels along the bound-
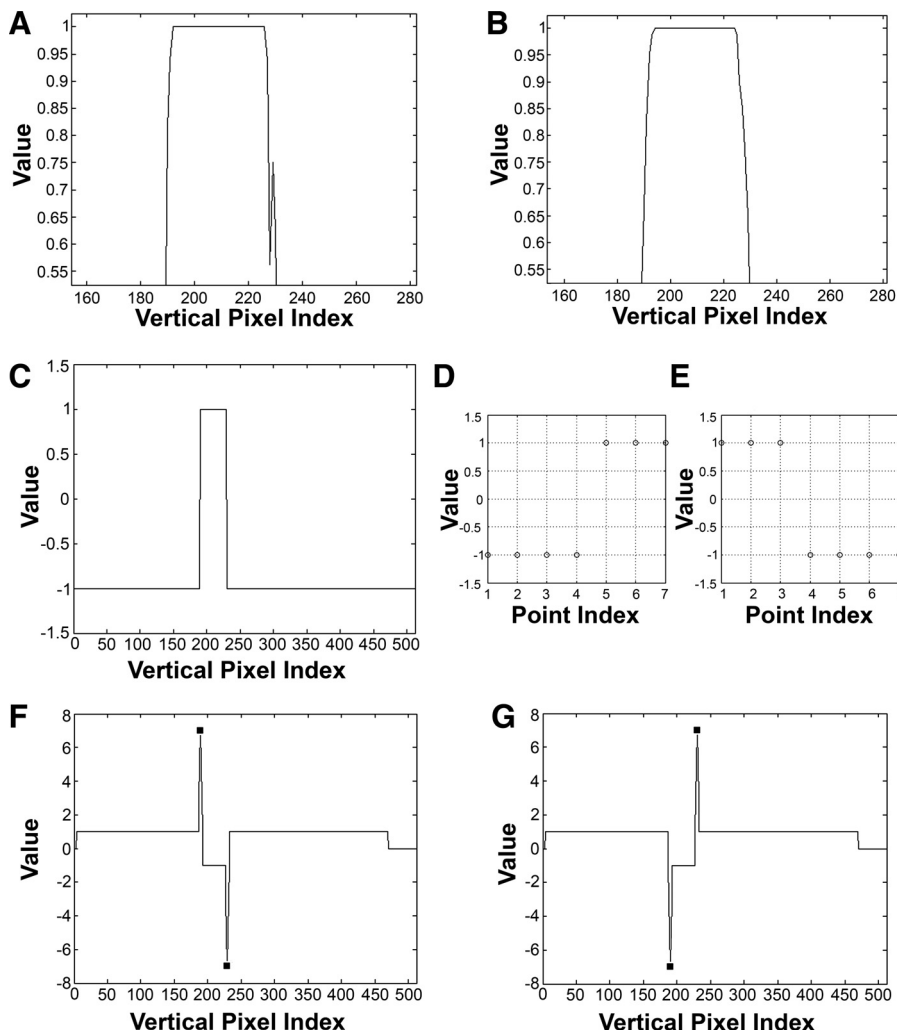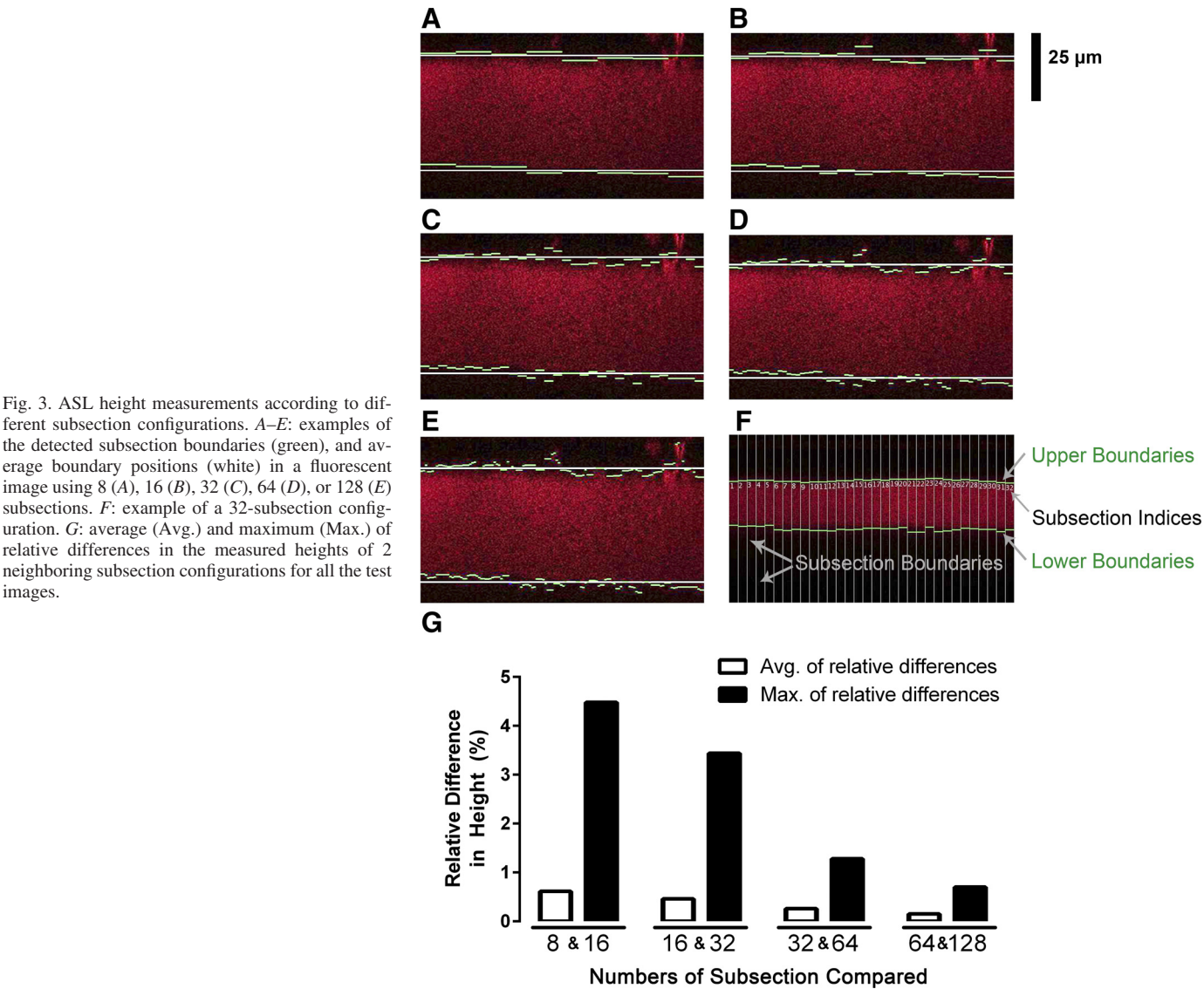

Fig. 2. Analysis of histogram profiles using a 7-step filter. *A*: histogram profile of *subsection 2* (taken from Fig. 1*C*). *B*: histogram showing the result of a 5-point running average. *C*: bipolar profile after thresholding of Fig. 1*C*. *D* and *E*: after application of 7-point step function, values are shown either as 1 or −1. *D* shows the rising edge and *E* shows the falling edge. *F*: graph showing the result of filtering with the 7-point rising edge step function. *G*: graph showing the result of filtering with the 7-point falling edge step function.

Fig. 3. ASL height measurements according to different subsection configurations. *A–E*: examples of the detected subsection boundaries (green), and average boundary positions (white) in a fluorescent image using 8 (*A*), 16 (*B*), 32 (*C*), 64 (*D*), or 128 (*E*) subsections. *F*: example of a 32-subsection configuration. *G*: average (Avg.) and maximum (Max.) of relative differences in the measured heights of 2 neighboring subsection configurations for all the test images.

aries of the ASL. By doing so, detected ASL boundaries were smoothed out (25, 37). The application of this series of algorithms resulted in the image shown in Fig. 1*C*, which has no noisy pixels on its boundaries.

After getting a binarized image to which Otsu's threshold and the morphological operations were applied, the boundaries of the foreground were found by histogram analysis. To deal with varying boundaries, the foreground region was divided into a number of horizontal subsections. Then the pixel values of each subsection were horizontally accumulated to give the pixel value index (*x*-axis) on a histogram profile. Figure 1*C* shows the subsections, and Fig. 1, *D–G* shows the corresponding histogram profiles. The upper and the lower boundaries of

a subsection correspond to the increasing and decreasing part of the histogram profile, respectively, within a range between 0 and 1 as listed on the *y*-axis of a histogram profile. The midrange value of 0.5 was applied as the histogram profile threshold to get the upper and lower boundaries of each subsection. To prevent processing failures due to noisy bounce, which is a phenomenon where the background is mistakenly read as the foreground and vice versa, we performed a preprocessing step using a five-point moving average to eliminate the noisy bounce of the profile (Fig. 2, *A* and *B*) (16, 25). The five-point moving average is a calculation that analyzes each pixel by creating a series of averages of the neighboring five pixels (2). With this calculation, anything less than five pixels

Table 1. *The average of elapsed times to measure ASL height of an image in the test image set according to the subsection configuration*

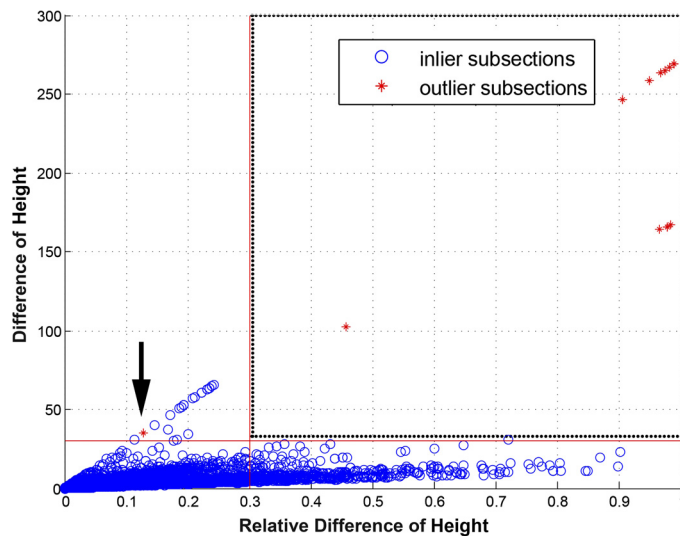| Subsection Configuration	8 Subsections	16 Subsections	32 Subsections	64 Subsections	128 Subsections
Elapsed time	22.8 ms	27.4 ms	36.3 ms	56.1 ms	91.5 ms

ASL, airway surface liquid.

Fig. 4. Distribution of inlier and outlier subsections in a 2-dimensional plane. Difference of height is the absolute value of the difference between the height of subsection and the initial average of heights. Relative difference of height is the absolute value of the difference between the height of a subsection and the initial average of heights divided by the initial average of heights. The ground truth inliers (blue circles) and outliers (red asterisks) are suboptimally separated by union of the 2 thresholded regions bounded by the red lines. Therefore, any subsections located within the dotted square are considered outliers. In the process of defining inliers and outliers, inaccurate selection occurred as shown here at point ∼(0.12, 40; see arrow). However, the accuracy of the mean ASL height was not altered because our algorithm is dependent on the distribution of all collected data points.

was regarded as an artifact. Following the noise reduction, the same threshold of 0.5 was applied to obtain a bipolar profile (Fig. 2C); bipolar profiles assign 1 to the parts above the threshold and −1 to the parts below the threshold.

Filtering is a type of processing used to detect the exact location of the signal. Here, we used a filtering technique to detect the exact location of the ASL boundaries, namely, seven-point filtering, which is a type of image analysis meth-

odology based on seven pixels. Seven-point filtering consists of $A = [-1 \; -1 \; -1 \; -1 \; 1 \; 1 \; 1]$ for the rising edge detection, a location where the ASL region begins, and $B = [1 \; 1 \; 1 \; -1 \; -1 \; -1 \; -1]$ for the falling edge, a location where the ASL region ends (Fig. 2, D and E). Upon experimental analysis, we found that any filtering below seven pixels was unable to deal with the noisy peaks produced on the edges of ASL. On the other hand, filtering above seven pixels was unnecessary because 1) the results did not improve any further and 2) the increased filtering slowed the analysis speed. Thus, to maximize the speed of our algorithm while maintaining accuracy, we decided to use seven-point filtering.

The trace in Fig. 2F represents a rising edge that was characterized by having the first peak with a value of +7 and the second peak with a value of −7. The value of +7 from Fig. 2F occurs when the fifth value of *filter A* (+1) is aligned with the first location from the left where the bipolar profile value is +1. This results in the equation $(-1 \cdot -1) + (-1 \cdot -1) + (-1 \cdot -1) + (-1 \cdot -1) + (1 \cdot 1) + (1 \cdot 1) + (1 \cdot 1) = +7$. Differently put, it is where the first location from the left in Fig. 2C that returns a value of +1 is aligned with the *point index 5* with a value of +1 in Fig. 2D. The −7 peak from Fig. 2F is returned when the fourth integer of *filter A* (−1) is aligned with the last location from the left where the bipolar profile value is +1 in the equation $(-1 \cdot 1) + (-1 \cdot 1) + (-1 \cdot 1) + (-1 \cdot 1) + (1 \cdot -1) + (1 \cdot -1) + (1 \cdot -1) = -7$. In other words, it is where the first value of +1 from the right in Fig. 2C is aligned with the *point index 4*, which returns a value of −1 in Fig. 2D. Conversely, the graph in Fig. 2G represents a falling edge that is characterized by having its first peak with a value of −7, followed by a second peak with a value of +7. These values are produced by using the same logic of finding the rising edge. The first peak with a value of −7 occurs when the fourth value of *filter B* (−1) and is aligned with the first point from the left where the bipolar profile value is 1. This results in the equation $(1 \cdot -1) + (1 \cdot -1) + (1 \cdot -1) + (-1 \cdot -1) + (-1 \cdot 1) + (-1 \cdot 1) + (-1 \cdot 1) = -7$. The second peak with a value of 7 occurs when the third value of the
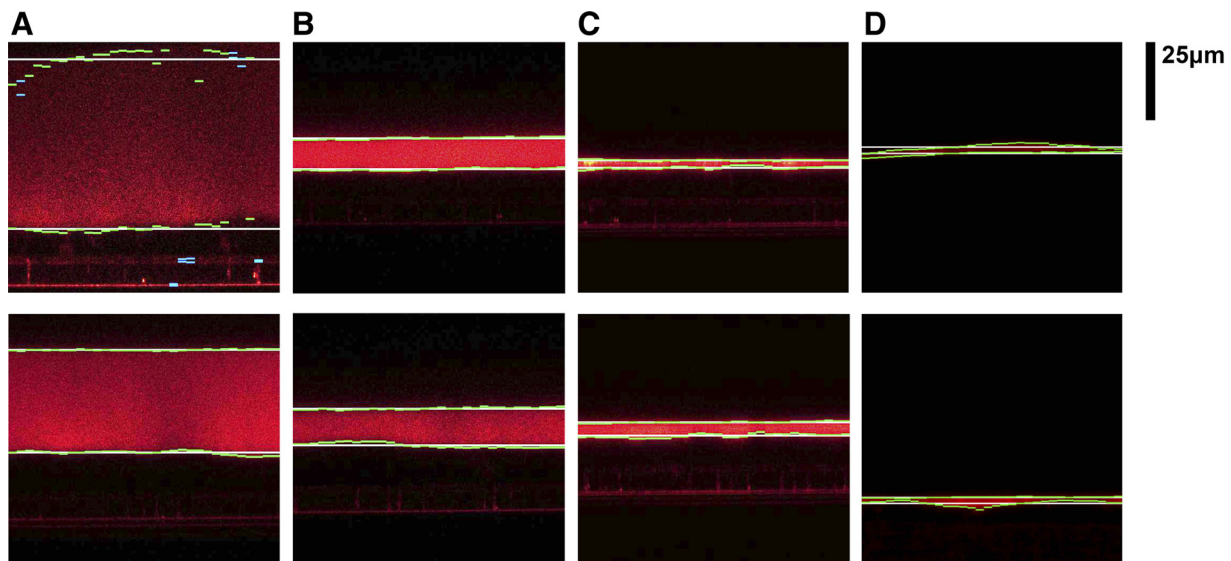

Fig. 5. Examples of the detected boundaries of different ASL regions obtained from the test image set. A: broad ASL region. B: moderate ASL region. C: narrow ASL region from normal human bronchial epithelial cultures (HBECs). D: very narrow ASL region from cystic fibrosis (CF) HBECs. The thickness of the ASL band did not affect the detection of accurate boundaries (green lines), average boundaries (white line), and outlier subsections (blue).

filter B (+1) is aligned with the first point from the right where the bipolar profile value is 1 in the equation $(1 \cdot 1) + (1 \cdot 1) + (1 \cdot 1) + (-1 \cdot -1) + (-1 \cdot -1) + (-1 \cdot -1) + (-1 \cdot -1) = +7$. Therefore, Fig. 2*G* represents the alignment between Fig. 2, *C* and *E*.

Occasionally, the boundaries could not be found in some subsections. This typically occurred when the ASL region was either very narrow or unclear. Since the HBECs represent a heterogeneous cell population of varying height and composition, and since the inverted confocal must scan through the cells to image the ASL, this sometimes occurs during acquisition. In these cases, the subsections without boundaries were excluded from further processing. Our studies indicated that omitting some subsections did not affect the final height calculation since the total number of remaining subsections was more than sufficient to calculate the mean ASL height.

Finding the optimal number of subsections. Figure 3, *A–E* shows the analyzed ASL height images according to the specific number of subsections. The number of subsections directly affects the detected boundaries of the ASL region and hence the measured height. Although the number of subsections can be increased for more accurate boundary detection, the number should not be more than 128, because in such a case the width of a subsection decreases to ≤ 3 pixels, and the analysis of the histogram profiles becomes unreliable. Moreover, increasing the number of subsections decreases the speed of analysis (Table 1). The maximum difference of the measured heights between 8 and 16 subsections was 4.48% and that of 16 and 32 subsections was 3.44% (Fig. 3*G*). However, the maximum difference of the measured heights between 32 and 64 subsections was 1.28%, a value small enough to dismiss without any expectation to dramatically increase the accuracy of the result (Fig. 3*G*). Since the purpose of the subsections is not to find exact boundaries of the ASL region but to calculate a representative ASL height, no more than 32 subsections is necessary. Therefore, for the optimal number of subsections, we decided to use 32 subsections of 16-pixel width (Fig. 3*F*).

Finding valid subsections. There is a possibility that detected boundaries within the subsections may not be real owing to computational detection errors. Furthermore, when a cell dies, the space occupied by that cell may fill the fluorescent dextran, which may cause additional artifact. To avoid using these invalid artifactual boundaries, we decided to find an optimal threshold for excluding outlier subsections. All of the subsections were independently considered as a sample of data in two-dimensional feature space of the relative difference and the absolute difference of height. The absolute difference of height was calculated as the difference between the height of a

subsection and the initial average height of the median 60% of all subsections. In practice, we found that when $\geq 50\%$ of the ASL regions were noisy, the ASL height analysis was unsuccessful and the data was mostly artifactual. However, when 40% or less of the ASL regions contained noise, then the ASL height analysis was consistently successful. Therefore, to maximize the selection of real ASL heights, while cautiously filtering out any artifacts, we used a median 60% threshold. The relative difference of height is calculated as the ratio of the absolute difference to the initial average height. Figure 4 shows the distribution of all subsections of the test image set in the feature space. Blue circles and red asterisks represent the ground truth inliers and outliers, respectively. Although inliers and outliers are not completely separable in this feature space as seen in the graph, we can select suboptimal threshold values for each dimension. The vertical and the horizontal red lines represent the relative difference threshold of 0.3 and the absolute difference threshold of 30 pixels, respectively. We selected these values to tightly restrict the inlier boundary to minimize the loss of inliers while precisely excluding outliers. In the process of defining inliers and outliers, inaccurate selection of outliers rarely occurs. However, an example of a rare included outlier is shown at point $\sim(0.12, 40)$ in Fig. 4 (see arrow). Moreover, the accuracy of the mean ASL height is not tempered since our algorithm is not dependent on individual data points and rather is an aggregate of the data set.

Our automatic analysis was performed on ASL images obtained from normal and CF HBECs; and the final output of the image analysis and the subsequent ASL height measurements are shown in Fig. 5 and Table 2. Using our method, we were able to detect extremely thin ASL regions from CF HBECs. As such, the minimum required for our algorithm to successfully detect ASL was four pixels in height.

Finding the optimal Mark-and-Find design. We next acquired *XZ* scanned images for each culture using the Mark-and-Find function on a Leica SP8 confocal microscope equipped with an automatic stage. The Mark-and-Find function allows the user to save multiple predetermined locations and then to acquire images. Harvey and colleagues (13) have previously shown that the edges of the cultures do not represent a thin film ASL because of a meniscus that exists between the culture and the plastic sidewall of the culture insert. According to their work, anything outside ~ 0.6 mm from the edge can be counted as "thin film" when using 12-mm-diameter Transwell culture inserts (13). We designed five different Mark-and-Find protocols, ranging from 5 to 40 saved locations per protocol (Fig. 6*A*), and all locations for our Mark-and-Find functions

Table 2. *Result of height measurements with 32 subsections and the representative ASL heights of the test image set obtained by using our program*

Image Name*	Average of Inliers, pixels/μm	Subregion†					
		Subregion1, pixels/μm	Subregion2, pixels/μm	Subregion3, pixels/μm	Subregion30, pixels/μm	Subregion31, pixels/μm	Subregion32, pixels/μm
1.jpg	70.94/19.40	62/16.95	62/16.95	69/18.87	63/17.23	65/17.77	67/18.32
2.jpg	86.10/23.54	78/21.33	81/22.15	81/21.15	85/23.24	87/23.79	83/22.70
3.jpg	78.13/21.36	87/23.79	89/24.34	87/23.79	76/20.78	78/21.32	81/22.15
4.jpg	57.00/15.59	40/10.94	38/10.39	41/11.21	66/18.05	66/18.05	64/17.50
211.jpg	15.47/4.23	13/3.55	13/3.55	13/3.55	22/6.02	21/5.74	22/6.02
212.jpg	16.03/4.38	23/6.29	22/6.02	20/5.47	15/4.10	19/5.20	23/6.29

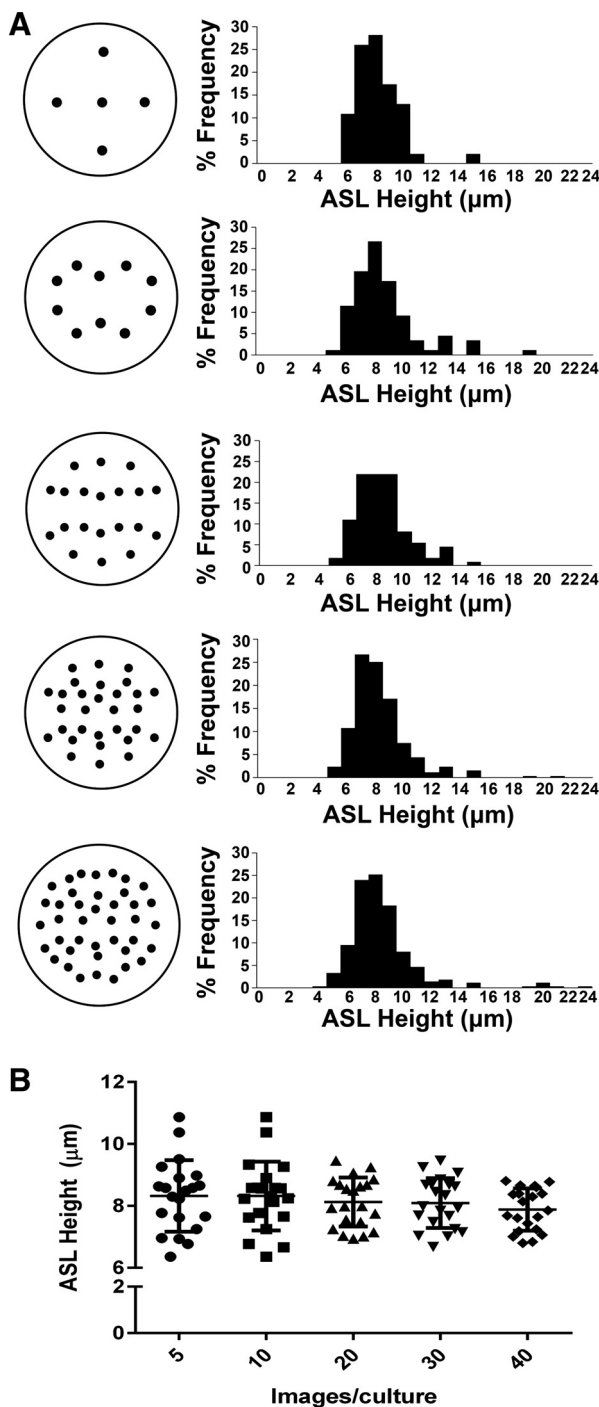*Images 5–210 not shown. †Subregions 4–29 not shown.

Fig. 6. A comparison of sample size vs. mean ASL height. *A*: Mark-and-Find designs for acquiring different amounts of fluorescent images per culture (*left*). Each dot represents a location where an image is acquired. Histograms of measured ASL heights from all of the acquired images corresponding to Mark-and-Find designs using *n* = 5–40 images per culture (*right*). *B*: graph showing mean ASL heights vs. the number of data points used, based on the different Mark-and-Find designs shown in *A*. Each data point represents a mean ASL height from each culture. The same cultures were reimaged by using each of the 5 different Mark-and-Find algorithms.

was an increase in the ASL volume due to the addition of the liquid vehicle (20 μl PBS). We found that ASL absorption to the steady-state level of ~7 μm took ~4 h. Therefore, we acquired ASL images 4 h after the loading of the dye to look at the distribution of ASL heights. All the images acquired for each of the Mark-and-Find designs were analyzed by our proposed automatic analysis method to obtain ASL heights and the data set was plotted as histograms (Fig. 6*A*). From the histograms, it appeared that the recorded ASL heights were not normally distributed (Fig. 6*A*). Further analysis using D'Agostino and Pearson's omnibus normality test revealed that all of the data sets had *P* values <0.0001, indicating that they failed to pass the normality test and were skewed.

To obtain a mean ASL height for each culture, ASL heights recorded for the saved locations for each Mark-and-Find design were averaged. The most representative ASL height of a culture is obtained when the marked locations densely covered the entire culture and the images acquired at those locations were analyzed. Therefore, within our Mark-and-Find designs, the most representative ASL height was obtained by using the 40 images/culture design to give an averaged ASL height (Fig. 6*A*). Figure 6*B* shows distribution of the averaged ASL heights obtained for each of the Mark-and-Find design. Each data point in Fig. 6*B* represents a mean ASL height from each culture. The same cultures were reimaged using each of the five different Mark-and-Find algorithms. The distribution of the average ASL heights was wider when fewer images were taken per culture (Fig. 6*B*). The mean values of the averaged ASL heights were 8.32 ± 1.15, 8.17 ± 1.11, 8.13 ± 0.79, 8.09 ± 0.80, and 7.88 ± 0.86 μm for 5, 10, 20, 30, and 40 images/culture design, respectively (Fig. 6*B*).

Application of the proposed automated method. We have previously shown that SPLUNC1 hydrates ASL by inhibiting ENaC (12, 14) and that when washed away it takes ~12 h for endogenous SPLUNC1 to return to the ASL and to regulate ENaC (14). Taking advantage of our automatic ASL measurement method, we produced a time course for ASL absorption and a dose-response curve after the treatment of recombinant SPLUNC1 on HBECs. (all *n* = 24). To eliminate the effect of endogenously secreted SPLUNC1, we washed each culture apically with 500 μl PBS prior to the loading of 20 μl tetramethylrhodamine-dextran mixed with varying concentrations of SPLUNC1. Immediately after loading of the dye, ASL height was found to be ~25 μm. Over the next 8 h, ASL was absorbed by ENaC-mediated ion transport. Increasing the concentration of SPLUNC1 in the ASL increased steady-state ASL height (Fig. 7*A*). However, the first time point to see the significant difference in the hydration state of ASL was at 4 h. Therefore, we selected this time to perform a dose response of the effect of SPLUNC1 on ASL height. The ASL height with 1 μM SPLUNC1 after 4 h was 9.00 ± 0.48 μm, and at this concentration ASL height was significantly different from all the lower dosages ($P < 0.05$; Fig. 7*B*). The average ASL height continued to increase significantly with increasing concentrations of SPLUNC1 (Fig. 7*B*). Treatment with 10, 25, and 100 μM SPLUNC1 resulted in the measured ASL height of 9.95 ± 0.21, 11.94 ± 0.50, and 11.75 ± 0.54 μm, respectively. (Fig. 7*B*). The IC_{50} of SPLUNC1 was 6.53 μM.

To test whether our automated analysis approach could be applied to other confocal systems, we obtained images from normal and CF HBECs using a Zeiss 510 confocal microscope
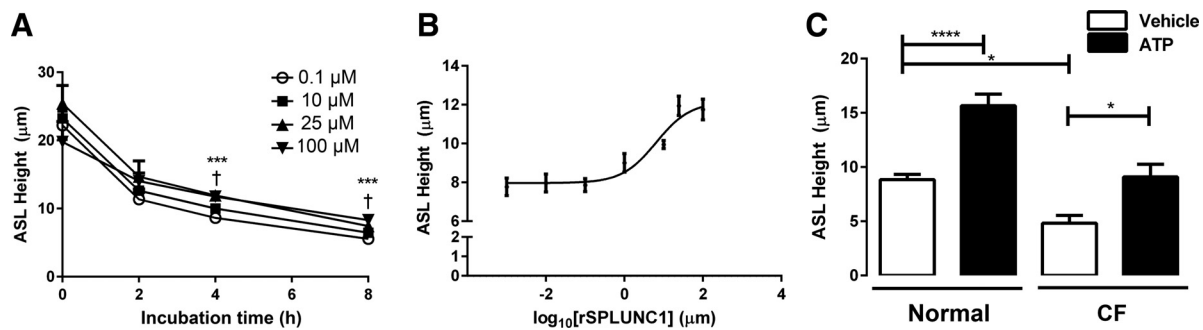
were designed to avoid the meniscus-containing edges of the cultures. An automatic stage positioned each culture to pre-saved locations to acquire one image per location at a rate of ~1 image/s. Immediately after the loading of the dye, there

Fig. 7. Validation of our approach: inhibition of ENaC and stimulation of CFTR/Cacc on ASL height. *A*: ASL height in the presence of varying concentrations of recombinant SPLUNC1 (all $n = 24$). Compared with 0.1 μM: ***$P < 0.001$, difference to 100 μM. †$P < 0.05$, difference to 10 and 25 μM. *B*: dose response for ASL height following 4-h recombinant SPLUNC1 exposure on HBECs (all $n = 28$). *C*: ASL height in the presence and absence of 300 μM of ATP on normal and CF HBECs ($n = 30$ for normal and $n = 20$ for CF). ****$P < 0.0001$ and *$P < 0.05$.

that was equipped with a manual stage. Analysis of data acquired in this fashion revealed a significant difference in ASL height between normal and CF HBECs (Fig. 7*C*). We then activated Cl^-/ASL secretion by exposing these HBECs to ATP, which was added as a dry powder in perfluorocarbon (30). For normal HBECs, addition of 300 μM ATP significantly increased the ASL height from 8.85 ± 0.49 to 15.66 ± 1.06 μm. For CF cultures, the same ATP stimulation significantly increased ASL height from 4.82 ± 0.72 to 9.09 ± 1.16 μm (Fig. 7*C*).

DISCUSSION

Understanding the physiology that underlies ASL volume regulation may help to develop therapeutic agents for the treatment of obstructive lung diseases such as CF and COPD in which ASL/mucus dehydration is an issue. ASL height measurements by confocal microscopy have been widely used to study the regulation of ASL height by airway epithelia and have revealed that maintaining hydrated ASL by correctly modulating ENaC and CFTR activity maintains efficient mucus transport (20, 26, 30). Moreover, this technique has been used to investigate the efficacy of therapeutic agents for CF and COPD (3, 30, 34). To reduce the time burden of manually acquiring and analyzing ASL images, we have designed a novel automatic image acquisition and analysis method. With this technique, image acquisition and analysis were relatively easy, quick, and unbiased.

Our algorithm requires 60% of the ASL region to be detected to set inlier and outlier boundaries. In our cell culture system, it is not difficult to meet this requirement. For a more robust elimination of outlier subsections, the RANSAC (Random Sample Consensus) technique can be applied instead of using median 60% of subsections (9). RANSAC randomly selects subsections to create a pool of inliers and therefore does not require a large amount of inliers to eliminate outliers. However, this process needs a very long time to search all of the inliers and outliers, especially when inliers are small. So the computational cost of RANSAC is higher than the median technique of the proposed measuring algorithm. This is a tradeoff between computational cost and robustness.

The analysis algorithms were compiled by using MATLAB code for fast prototyping. Currently, the average processing time from binarizing a fluorescence image to calculating a representative height of ASL using 128 subsections only takes

several tens of milliseconds on a laptop with a single thread of Intel i7 2.4 GHz CPU (Table 1). The analysis can be performed on any images as long as the ASL is shown in red. For other colors, the threshold for selecting the foreground must be changed. If this program is converted to C code, then the program will run 5 to 10 times faster, bringing the processing time down to several milliseconds, owing to C compiler's optimal characteristics. This superfast speed may be advantageous when dealing with even larger quantities of fluorescence images.

When our proposed automated image analysis with 32 subsections as a parameter was used to measure ASL height, the values repeatedly remained the same and there was no error in computation or no exceptional failure in running the algorithm of the proposed measuring techniques (Table 2). Our measurement method accurately found the real boundaries (green lines), average of boundaries (white), and the outlier subsections (blue) in all conditions where the height of ASL, brightness of the image, and the clarity of the boundaries varied from image to image (Fig. 5). Moreover, our method can read ASL images from different types of microscopes, and with different lenses, so long as the ASL region is shown using a standard 8- or 16-bit grayscale look-up table. Although the threshold parameters are experimentally determined, in the case of ASL images with dimmer fluorescent labeling, those parameters can easily be modified, e.g., multiplying each image by a suitable integer (e.g., 2) by using a program such as Image J (NIH Freeware), which only has a small effect on the background, can enhance the foreground/ASL image.

When comparing different Mark-and-Find designs, the distribution of the raw data set as well as representative averaged ASL heights did not show much difference (Fig. 6). That is, the mean values of the averaged ASL heights among difference Mark-and-Find designs were not statistically different from one another (Fig. 6*B*). Interestingly, 5 and 10 images per culture both returned standard deviations > 1.0 (1.15 and 1.11, respectively), whereas 20, 30, and 40 images/culture gave standard deviation values <1.0 (0.79, 0.80, and 0.86, respectively). Therefore, we concluded that although using the design of 5 images per culture produced a sufficiently reliable data set, the most precise data set for ASL height measurement was obtained when acquiring 20 images/culture. Additionally, since HBECs can vary in cell layer thickness, even within one culture, it sometimes happens that one to two images per

culture are out of the field of view and/or unreadable. However, even with this error rate, this still leaves enough ASL images to perform a thorough analysis, and in the interest of through-put we have found that it is better to discard unusable images rather than to try to reimage them.

Using our method, we were able to rapidly generate a time course to show that SPLUNC1's ability to inhibit ENaC lasted for 8 h and a dose-response curve to show that the maximum efficacy of SPLUNC1 for inhibiting ENaC was at 25 μM and with an IC_{50} of 6.53 μM (Fig. 7, A and B). We were also able to demonstrate that our program can detect differences in ASL height between normal and CF HBECs. As previously described (20), basal ASL height was significantly different in normal compared with CF HBECs (Fig. 7C). We next tested whether our method could detect changes in ASL height following the activation of Cl^- secretion with mucosal ATP. Both normal and CF HBECs elicited a significant response to ATP (Fig. 7C). However, the magnitude of the response was significantly greater in normal and CF HBECs (Fig. 7C). ATP is rapidly metabolized to adenosine by ectoenzymes in the ASL (18). As such, ATP and its breakdown product adenosine are predicted to activate CaCC and CFTR, respectively, in normal airway epithelia. In contrast, ATP can activate CaCC in CF HBECs, and although adenosine is likely still formed, adenosine's effector (CFTR) is absent from CF HBECs.

For this paper, we automatically acquired ASL images from one 12-mm-diameter culture at a time, which was placed in a chamber on the inverted confocal microscope prior to imaging. Although our method can be theoretically applied to cultures placed in 12-well dishes or in other multiwell systems, the cultures would need to be sufficiently close to the bottom of the chamber to stay within the working distance of the objective lens (our ×63 glycerol objective lens has a working distance of 300 μm). When cultures are placed in commercially available 12-well plates, the distance between the objective lens and the ASL exceeds this range and the ASL cannot be imaged. However, should new 12-, 24-, or 96-well plates become available that were redesigned to place the cultures closer to the lens, then our technique could be modified appropriately, which would be predicted to significantly increase the through-put of the imaging.

In conclusion, our automatic ASL measurement method combines the usage of an automatic stage on a XZ-scanning confocal microscope for ASL image acquisition and a novel code for automatic image analysis of ASL heights. We have shown here that our method generates ASL height measurements with consistency, accuracy, and speed without the need for extensive computing power. Our method will increase the throughput of ASL measurements, which can be applied for a fast screening of therapeutic drugs and for the study of airway physiology. All the codes and program will soon be released online at http://pogary.yu.ac.kr.

DISCLOSURES

No conflicts of interest, financial or otherwise, are declared by the author(s).

AUTHOR CONTRIBUTIONS

H.-C.C., C.S.K.K., and R.T. conception and design of research; H.-C.C., C.S.K.K., and R.T. performed experiments; H.-C.C. and C.S.K.K. analyzed data; H.-C.C., C.S.K.K., and R.T. interpreted results of experiments; H.-C.C. and C.S.K.K. prepared figures; H.-C.C. and C.S.K.K. drafted manuscript; H.-C.C. and R.T. approved final version of manuscript; C.S.K.K. and R.T. edited and revised manuscript.

REFERENCES

1. **Althaus M.** ENaC inhibitors and airway re-hydration in cystic fibrosis: state of the art. *Curr Mol Pharmacol* 6: 3–12, 2013.
2. **Arce G.** *Nonlinear Signaling Processing: A Statistical Approach.* Hobo-ken, NJ: Wiley, 2005.
3. **Astrand ABM, Hemmerling M, Root J, Wingren C, Pesic J, Johans-son E, Garland AL, Ghosh A, Tarran R.** Linking increased airway hydration, ciliary beating, and mucociliary clearance through ENaC inhi-bition. *Am J Physiol Lung Cell Mol Physiol* 308: L22–L32, 2015.
4. **Boucher RC.** Airway surface dehydration in cystic fibrosis: pathogenesis and therapy. *Annu Rev Med* 58: 157–170, 2007.
5. **Boucher RC.** Molecular insights into the physiology of the "thin film" of airway surface liquid. *J Physiol* 3: 631–638, 1999.
6. **Chambers LA, Rollins BM, Tarran R.** Liquid movement across the surface epithelium of large airways. *Respir Physiol Neurobiol* 159: 256–270, 2007.
7. **Choi HC, Oh SY.** Face detection in static images using Bayesian discriminating feature and particle attractive genetic algorithm. *2005 IEEE/RSJ Int Conf Intell Robot Syst IROS* 2005: 3616–3621, 2005.
8. **Cohen-Cymberknoh M, Kerem E, Ferkol T, Elizur A.** Airway inflam-mation in cystic fibrosis: molecular mechanisms and clinical implications. *Thorax* 68: 1157–1162, 2013.
9. **Fischler M, Bolles R.** Random sample consensus: a paradigm for model fitting with applications to image analysis and automated cartography. *Commun ACM* 24: 381–395, 1981.
10. **Fulcher ML, Randell SH.** Human nasal and tracheo-bronchial respiratory epithelial cell culture. *Methods Mol Biol* 945: 109–121, 2013.
11. **Garcia-Caballero A, Rasmussen JE, Gaillard E, Watson MJ, Olsen JC, Donaldson SH, Stutts MJ, Tarran R.** SPLUNC1 regulates airway surface liquid volume by protecting ENaC from proteolytic cleavage. *Proc Natl Acad Sci USA* 106: 11412–11417, 2009.
12. **Garland AL, Walton WG, Coakley RD, Tan CD, Gilmore RC, Hobbs CA, Tripathy A, Clunes LA, Bencharit S, Stutts MJ, Betts L, Redinbo MR, Tarran R.** Molecular basis for pH-dependent mucosal dehydration in cystic fibrosis airways. *Proc Natl Acad Sci USA* 110: 15973–15978, 2013.
13. **Harvey PR, Tarran R, Garoff S, Myerburg MM.** Measurement of the airway surface liquid volume with simple light refraction microscopy. *Am J Respir Cell Mol Biol* 45: 592–599, 2011.
14. **Hobbs CA, Blanchard MG, Alijevic O, Tan CD, Kellenberger S, Bencharit S, Cao R, Kesimer M, Walton WG, Henderson AG, Red-inbo MR, Stutts MJ, Tarran R.** Identification of the SPLUNC1 ENaC-inhibitory domain yields novel strategies to treat sodium hyperabsorption in cystic fibrosis airway epithelial cultures. *Am J Physiol Lung Cell Mol Physiol* 305: L990–L1001, 2013.
15. **Jayaraman S, Song Y, Vetrivel L, Shankar L, Verkman AS.** Nonin-vasive in vivo fluorescence measurement of airway-surface liquid depth, salt concentration, and pH. *J Clin Invest* 107: 317–24, 2001.
16. **Kenney JF, Keeping ES.** Moving averages. In: *Mathematics of Statistics* (3rd ed.). New York: Van Nostrand, vol. 1, p. 221–223, 1954.
17. **Kunzelmann K, Schreiber R.** Airway epithelial cells—hyperabsorption in CF? *Int J Biochem Cell Biol* 44: 1232–1235, 2012.
18. **Lazarowski ER, Boucher RC.** Purinergic receptors in airway epithelia. *Curr Opin Pharmacol* 9: 262–267, 2009.

19. **Liu L, Chu KK, Houser GH, Diephuis BJ, Li Y, Wilsterman EJ, Shastry S, Dierksen G, Birket SE, Mazur M, Byan-Parker S, Grizzle WE, Sorscher EJ, Rowe SM, Tearney GJ.** Method for quantitative study of airway functional microanatomy using micro-optical coherence tomography. *PLoS One* 8: e54473, 2013.

20. **Matsui H, Grubb BR, Tarran R, Randell SH, Gatzy JT, Davis CW, Boucher RC.** Evidence for periciliary liquid layer depletion, not abnormal ion composition, in the pathogenesis of cystic fibrosis airways disease. *Cell* 95: 1005–1015, 1998.

21. **Matsui H, Randell SH, Peretti SW, Davis CW, Boucher RC.** Coordinated clearance of periciliary liquid and mucus from airway surfaces. *J Clin Invest* 102: 1125–1131, 1998.

22. **Otsu N.** A threshold selection method from gray-level histograms. *IEEE Trans Syst Man Cybernetics* 9: 62–66, 1975.

23. **Pilewski JM, Frizzell RA.** Role of CFTR in airway disease. *Physiol Rev* 79: 215–256, 1999.

24. **Schmid A, Clunes LA, Salathe M, Verdugo P, Dietl P, Davis CW, Tarran R.** Nucleotide-mediated airway clearance. *Subcell Biochem* 55: 95–138, 2011.

25. **Serra J, Soille P, editors.** *Mathematical Morphology and Its Applications to Image Processing*. Dordrecht, The Netherlands: Springer Science+ Business Media, 1994.

26. **Song Y, Namkung W, Nielson DW, Lee J, Finkbeiner WE, Verkman AS.** Airway surface liquid depth measured in ex vivo fragments of pig and human trachea: dependence on Na^+ and Cl^- channel function. *Am J Physiol Lung Cell Mol Physiol* 297: L1131–L1140, 2009.

27. **Tarran R, Boucher RC.** Thin-film measurements of airway surface liquid volume/composition and mucus transport rates in vitro. *Methods Mol Med* 70: 479–492, 2002.

28. **Tarran R, Button B, Boucher RC.** Regulation of normal and cystic fibrosis airway surface liquid volume by phasic shear stress. *Annu Rev Physiol* 68: 543–561, 2006.

29. **Tarran R, Grubb BR, Gatzy JT, Davis CW, Boucher RC.** The relative roles of passive surface forces and active ion transport in the modulation of airway surface liquid volume and composition. *J Gen Physiol* 118: 223–236, 2001.

30. **Tarran R, Grubb BR, Parsons D, Picher M, Hirsh AJ, Davis CW, Boucher RC.** The CF salt controversy□: in vivo observations and therapeutic approaches. *Mol Cell* 8: 149–158, 2001.

31. **Tarran R, Trout L, Donaldson SH, Boucher RC.** Soluble mediators, not cilia, determine airway surface liquid volume in normal and cystic fibrosis superficial airway epithelia. *J Gen Physiol* 127: 591–604, 2006.

32. **Thiagarajah JR, Song Y, Derichs N, Verkman AS.** Airway surface liquid depth imaged by surface laser reflectance microscopy. *J Gen Physiol* 136: 353–362, 2010.

33. **Thibodeau PH, Butterworth MB.** Proteases, cystic fibrosis and the epithelial sodium channel (ENaC). *Cell Tissue Res* 351: 309–323, 2013.

34. **Van Goor F, Hadida S, Grootenhuis PDJ, Burton B, Cao D, Neuberger T, Turnbull A, Singh A, Joubran J, Hazlewood A, Zhou J, McCartney J, Arumugam V, Decker C, Yang J, Young C, Olson ER, Wine JJ, Frizzell RA, Ashlock M, Negulescu P.** Rescue of CF airway epithelial cell function in vitro by a CFTR potentiator, VX-770. *Proc Natl Acad Sci USA* 106: 18825–18830, 2009.

35. **Van Goor F, Hadida S, Grootenhuis PDJ, Burton B, Stack JH, Straley KS, Decker CJ, Miller M, McCartney J, Olson ER, Wine JJ, Frizzell RA, Ashlock M, Negulescu PA.** Correction of the F508del-CFTR protein processing defect in vitro by the investigational drug VX-809. *Proc Natl Acad Sci USA* 108: 18843–18848, 2011.

36. **Verkman AS, Song Y, Thiagarajah JR.** Role of airway surface liquid and submucosal glands in cystic fibrosis lung disease. *Am J Physiol Cell Physiol* 284: C2–C15, 2003.

37. **Whittaker E, Robinson G.** *Calculus of Observations: A Treatise on Numerical Mathematics* (4th ed.). New York: Dover, 1967.

38. **Widdicombe JH.** Regulation of the depth and composition of airway surface liquid. *J Anat* 201: 313–318, 2002.

39. **Worthington EN, Tarran R.** Methods for ASL measurements and mucus transport rates in cell cultures. *Methods Mol Biol* 742: 77–92, 2011.

40. **Wu DX, Lee CY, Uyekubo SN, Choi HK, Bastacky SJ, Widdicombe JH.** Regulation of the depth of surface liquid in bovine trachea. *Am J Physiol Lung Cell Mol Physiol* 274: L388–L395, 1998.

41. **Zhang L, Button B, Gabriel SE, Burkett S, Yan Y, Skiadopoulos MH, Dang YL, Vogel LN, McKay T, Mengos A, Boucher RC, Collins PL, Pickles RJ.** CFTR delivery to 25% of surface epithelial cells restores normal rates of mucus transport to human cystic fibrosis airway epithelium. *PLoS Biol* 7: e1000155, 2009.

42. **Zhou Z, Duerr J, Johannesson B, Schubert SC, Treis D, Harm M, Graeber SY, Dalpke A, Schultz C, Mall MA.** The ENaC-overexpressing mouse as a model of cystic fibrosis lung disease. *J Cyst Fibros* 10, *Suppl* 2: S172–S182, 2011.